Check for updates

Few-layer WS₂ nanosheets with oxygen-incorporated defect-sulphur entrapped by a hierarchical N, S co-doped graphene network towards advanced long-term lithium storage performances†

Yan Wang, Xiaojun Zhao (ID)* and Zhi-Hong Liu (ID)*

Tungsten sulfide (WS₂) with two-dimensional layered graphene-like structure as an anode for lithium-ion batteries (LIBs) has attracted large attention owing to its high theoretical capacity and unique S–W–S layer structure. However, it also always suffers from poor electrical conductivity and volume expansion during lithiation/delithiation process in the practical application. Herein, we demonstrate the successful synergistic regulation of both structural and electronic modulation by simultaneous oxygen incorporation in defect-sulphur WS₂ nanosheets embedded into a conductive nitrogen and sulfur co-doped graphene framework (denoted as O-DS-WS₂/NSG), leading to dramatically enhanced lithium storage. Such a unique structure not only increases the accessible active sites for Li⁺ and enhances the kinetics of ion/electron transport, but also relieves the volume effect of WS₂. Furthermore, the surface defects and heteroatom incorporation can effectively regulate the electronic structure, improve the intrinsic conductivity and offer more active sites. Consequently, electrochemical performance results demonstrate that the obtained O-DS-WS₂/NSG nanocomposites possess great application prospects in LIBs with high specific capacity, superior rate performance as well as excellent cycle stability.

Introduction

Lithium-ion batteries (LIBs), as efficient and convenient electrical energy storage devices, are one of the most widely used based on their visible advantages with high energy density, high energy efficiency and long life time.[1–3] However, conventional graphite as the anode material for LIBs cannot keep pace with the gradually increasing energy consumption requirements.[4–6] It is, therefore, highly essential to develop alternative anode materials with excellent properties. Currently, transition metal sulfides such as WS₂, MoS₂, SnS₂, FeS₂, ReS₂ and CoS₂ (ref. 7–13) have been intensively reported owing to their high theoretical capacity stemming from their rich stoichiometric composition. Among these alternatives, WS₂ with two-dimensional (2D) individual sandwiched S–W–S layer structure has attracted extensive attention because of its high theoretical specific capacity of 432.6 mA h g⁻¹.[14,15] Nevertheless, there presents

many issues in terms of its poor electrical conductivity and severe capacity decay caused by huge volume change during fast Li⁺ insertion/desertion processes.[16,17] What is worse, WS₂ is especially easy to restack through van der Waals interactions between S–W–S layers, which severely compromises the electrochemical properties.[18]

To address the aforementioned disadvantages, one effective strategy is to combine WS₂ with carbonaceous material supports (carbon,[19] graphene,[20] carbon nanofibers[21] and carbon nanotubes,[22] etc.). These carbonaceous materials possess not only the high electron conductivity to accelerate electron transfer, but also provide large specific surface area to accommodate the large volume expansion and promote electrolyte penetration during lithium storage processes. Among various carbonaceous materials, graphene has attracted a lot of interest thanks to its high surface area, high electronic conductivity and flexibility.[23,24] Nevertheless, the inevitable aggregation of graphene greatly limits its intrinsic advantages in the decrease of conductivity and reduction of active sites.[25] Fortunately, 2D graphene and 2D WS₂ with similar layer structures present great geometric compatibility each other, which is in favor of constructing three-dimensional (3D) hierarchical graphene/WS₂ frameworks to over come the agglomeration.[18]

Additionally, optimizing intrinsic activity and boosting the intrinsic conductivity of compound by defect engineering and

Key Laboratory for Macromolecular Science of Shaanxi Province, School of Chemistry and Chemical Engineering, Shaanxi Normal University, Xi'an 710119, P. R. China. E-mail: xiaojunzhao@snnu.edu.cn; liuzh@snnu.edu.cn

† Electronic supplementary information (ESI) available: SEM, EDS mapping, TEM, XRD pattern, Raman, and BET of control samples; lithium storage comparison; rate capacities of NSG, WS₂/SG-800 and O-DS-WS₂/NC-800. See DOI: 10.1039/d0ra00558d

structure regulating have been considered to be another effective strategy. Rich defect structure could expose more active edge sites, afford stronger chemical interactions with active materials and accelerate ion/electron transport kinetic, thus resulting in an improved electrochemical performance.[26,27] For instance, the designed and synthesized bundled defect-rich MoS_2 or few-layer MoS_2/C nanosheets with rich defect has shown the superior rate capability and cycling ability as an anode material.[28,29] Nitrogen and halogen dual-doped graphene as an anode material in LIBs also reveals the outstanding reversible capacity and cycling stability.[30] Therefore, it is very important to rational design of unique 3D nanocomposite that is rich in defects to enhance the electrochemical performance of electrodes.

Herein, one-step thermal annealing strategy is firstly employed for the preparation of 3D architecture composed of oxygen incorporation in defect-sulphur WS_2 nanosheets and nitrogen and sulfur co-doped graphene framework (O-DS-WS_2/NSG). In the 3D O-DS-WS_2/NSG nanocomposites, O-DS-WS_2 nanosheets are evenly embedded into conductivity NSG support with high specific surface area. Apart from the advantages endowed by the 3D NSG frameworks, few-layer WS_2 nanosheets with oxygen incorporation and sulphur defect can afford more active sites to lithium storage and decrease Li^+ diffusion resistance. Benefiting from such merits, the as-obtained O-DS-WS_2/NSG nanocomposite as a LIBs anode material displays the high reversible specific capacities, excellent rate and cycling performances.

Experimental

Chemicals and materials

All reagents in these experiments were of analytical purity and used after purchase without further treatment. Graphene oxide (GO) was synthesized by improved Hummers' method.[31]

Synthesis of O-DS-WS_2/NSG nanocomposite

O-DS-WS_2/NSG nanocomposite was manufactured by a simple calcination method. Typically, 0.2 mL of aniline and 7 mg of sodium dodecyl sulfate were added in 50 mL of H_2O. Then 8.5 mL of aqueous GO dispersion (2.5 mg mL^{-1}) was added to the above solution and ultrasound for 30 min to form a homogeneous suspension. Subsequently, the solution of 0.5 g of $(NH_4)_2S_2O_8$ in 50 mL of HCl (1 mg mL^{-1}) was dropped slowly into above GO-containing dispersion, which was stirred for 24 h in an ice bath to obtain GO-polyaniline (GO-PANI). Afterward, adjust the pH to 6–8 with $NH_3 \cdot H_2O$. Then, 0.5 mmol of $Na_2WO_4 \cdot 2H_2O$ and 3.5 mmol of thiourea were added, stirred and freeze-dried. Finally, the as-prepared powder was calcined at different temperatures (650, 800, 950 °C) for 2 h in Ar with a ramping rate of 3 °C min^{-1}. After cooling to room temperature, the obtained black powder was collected by filtration and washed with deionized water several times to remove the impurities and dried at 60 °C in oven in vacuum overnight, which was labeled as O-DS-WS_2/NSG-650, O-DS-WS_2/NSG-800 and O-DS-WS_2/NSG-950, respectively. For comparison, pristine WS_2 was prepared by directly grinding $Na_2WO_4 \cdot 2H_2O$ and thiourea, then followed by calcination and washing with deionized water. In addition, O-DS-WS_2/N-doped carbon (O-DS-WS_2/NC-800), NSG, and WS_2/SG-800 nanocomposites were also synthesized using the above process at 800 °C except addition of the GO, $Na_2WO_4 \cdot 2H_2O$ and aniline, respectively.

Material characterization

The crystal structure of the as-obtained samples was characterized with a D8 Advance X-ray powder diffractometer (Cu Kα radiation with a step of 0.02° per second in the 2θ ranging from 10–80°). Raman spectra were obtained under visible light with wavelength 100–2000 cm^{-1} on in Via Reflex. The morphology and energy dispersive X-ray spectroscopy (EDS) mappings were characterized by a SU8220 field-emission scanning electron microscope (FESEM) equipped with an energy-dispersive spectrophotometer at an accelerating voltage of 5 kV. Transition electron microscopy (TEM), high-resolution transmission electron microscopy (HRTEM) images and SAED patterns were acquired on Tecnai G2 F20 (FEI) microscope. The surface compositions were analyzed using X-ray photoelectron spectrometer (XPS) on AXIS ULTRA (Kratos Analytical Ltd). Brunauer–Emmett–Teller specific surface area and the pore size distribution were acquired by N_2 adsorption/desorption isotherms measurement on ASAP 2460. Thermogravimetric analysis (TGA) curves were tested using TGA/DSC 3+ in air atmosphere from 25 to 800 °C with a heating rate of 10 °C min^{-1}, respectively.

Electrochemical measurements

The electrochemical performances were evaluated using CR2025 coin-type cell, the cells were assembled in an argon-filled glove box. Working electrode was prepared by mixing active materials, Super-P, and polyvinylidene fluoride with a mass ratio of 80 : 10 : 10 in N-methyl-2-pyrrolidone. The obtained slurry was spread on the Cu foil and dried in vacuum for 12 h (60 °C). The loading density of the active material is about 1.2–1.5 mg cm^{-2}. A Celgard 2400 membrane was used as the separator and the electrolyte was 1 M $LiPF_6$ in dimethyl carbonate/diethyl carbonate/ethylene carbonate (v/v/v, 1 : 1 : 1). The metal Li foil was a counter electrodes and reference electrode. Galvanostatic discharge–charge (GDC) curves were measured on a LANHE CT2001A battery testing system between 0.005 and 3 V. Cyclic voltammetry (CV) in a voltage window 0 to 3 V and electrochemical impedance spectrum (EIS) measurements with the frequency range of 100 kHz to 0.01 Hz of cells were performed by a CHI 760E electrochemical workstation (Chenhua, Shanghai).

Results and discussion

Fig. 1a illustrates our design idea for the preparation of O-DS-WS_2/NSG nanocomposite. The synthesis is started by mixing as-prepared GO-PANI, $Na_2WO_4 \cdot 2H_2O$ and thiourea under stirring, and freeze-dried. In this procedure, the electronegative WO_4^{2-} is firstly uniform anchored by the polyaniline (PANI) with
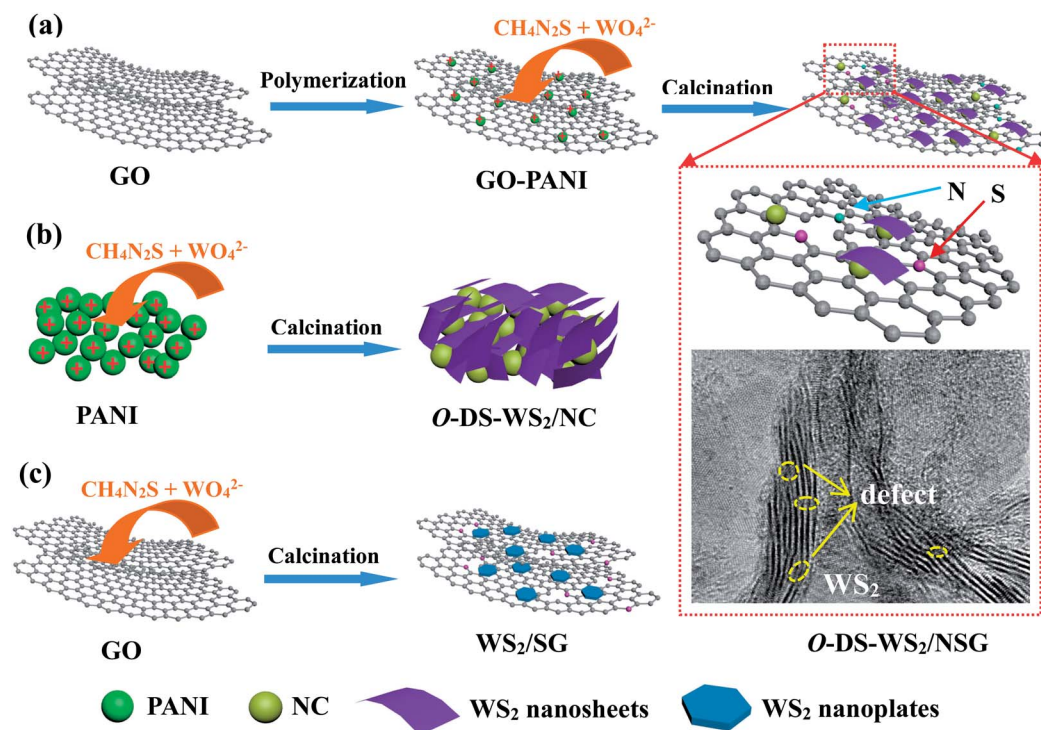
Fig. 1 Schematic illustration of the fabrication procedure of the O-DS-WS$_2$/NSG (a), O-DS-WS$_2$ (b) and WS$_2$/SG nanocomposites (c).

positive charge attached on the GO. Afterward, the obtained powder is subjected to the calcination treatment at different temperatures (650, 800, 950 °C) to form the few-layer O-DS-WS$_2$. The whole synthesis process for O-DS-WS$_2$/NSG is quite simple.

To understand the formation mechanism of few-layer WS$_2$ nanosheets, two control experiments are carried out without the addition of GO (Fig. 1b) or PANI (Fig. 1c), respectively. It is found that the obtained WS$_2$ nanosheets in the presence of PANI (O-DS-WS$_2$/NC) are consistent with those in the O-DS-WS$_2$/NSG-800 (Fig. S1a†). However, when the graphene is present, the WS$_2$ in WS$_2$/SG-800 (Fig. S1b†) shows an identical regular hexagon morphology, which suggests that the introduction of PANI is a key factor for the formation of few-layer WS$_2$ nanosheets. Therefore, we speculate that the formation of few-layer WS$_2$ may be attributed to the fact that the produced ammonium compounds during the high temperature process intercalate into the WS$_2$ layers and destroy the van der Waals interactions between S–W–S layers, thus leading to the thinner of WS$_2$.[32] Moreover, in this unique carbon matrix, graphene can play a powerful role to disperse PANI derived NC spheres (Fig. S1c and d†), which is convenient for few-layer WS$_2$ nanosheets uniformly anchored on the carbon substrate. Therefore, the synergistic effect among PANI, GO and WO$_4{}^{2-}$ ions allows the few-layer WS$_2$ to be evenly dispersed in the three-dimensional NSG network structure.

The morphologies and microstructures of the O-DS-WS$_2$/NSG at the different temperatures, WS$_2$/SG-800 and pristine WS$_2$ were analyzed by FESEM and TEM. The FESEM and TEM images of the O-DS-WS$_2$/NSG-800 (Fig. 2a and b) presents a 3D hierarchical sheet-like morphology, in which few-layer O-DS-

WS$_2$ nanosheets are uniformly embedded into the 3D NSG framework. The HRTEM image (Fig. 2c) reveals the broadened fringe spacing of about 0.66 nm, corresponding to the (002) lattice plane of 2H-WS$_2$, which mainly due to oxygen generated from the GO or WO$_4{}^{2-}$ ions partially replacing the normal sulfur lattice sites of WS$_2$ crystal.[33,34] The expanded interlayer spacing and few-layer feature can offer the more contact between WS$_2$ and electrolyte, facilitate insertion and extraction of Li$^+$ and shorten the transport paths of charge/ion during lithium storage process.[35,36] More importantly, O-DS-WS$_2$ nanosheets not only can reduce the band gap of WS$_2$ effectively to boost the intrinsic conductivity of WS$_2$, but also disorder atomic arrangement to further generate defect (marked by yellow dotted circles) structures along with the increase of active sites.[33,37–39] The selected-area electron diffraction (SAED) pattern of O-DS-WS$_2$/NSG-800 displays a set of diffraction bright rings, indexed to different crystal planes (002), (101), (103) and (110) of 2H-WS$_2$, respectively, indicating the high crystallinity of the O-DS-WS$_2$/NSG-800 (Fig. 2d). EDS elemental mapping images of O-DS-WS$_2$/NSG-800 (Fig. 2e–i) clearly indicate the presence of C, N, W, and S elements as well as they are all evenly distributed throughout the whole O-DS-WS$_2$/NSG-800 nanocomposites. Furthermore, EDS elemental mapping images of NSG (Fig. S2†) also confirm the coexistence of N, S in the graphene support, indicating the successful doped N and S atoms into the graphene. Compared to O-DS-WS$_2$/NSG nanocomposites, pristine WS$_2$ nanosheets with hexagonal nanoplate (an average size of about 100 nm and a thicker of about 25 nm) exhibit the serious aggregation morphology (Fig. S3a and b†). To further explore the effect of temperature on the morphology of the
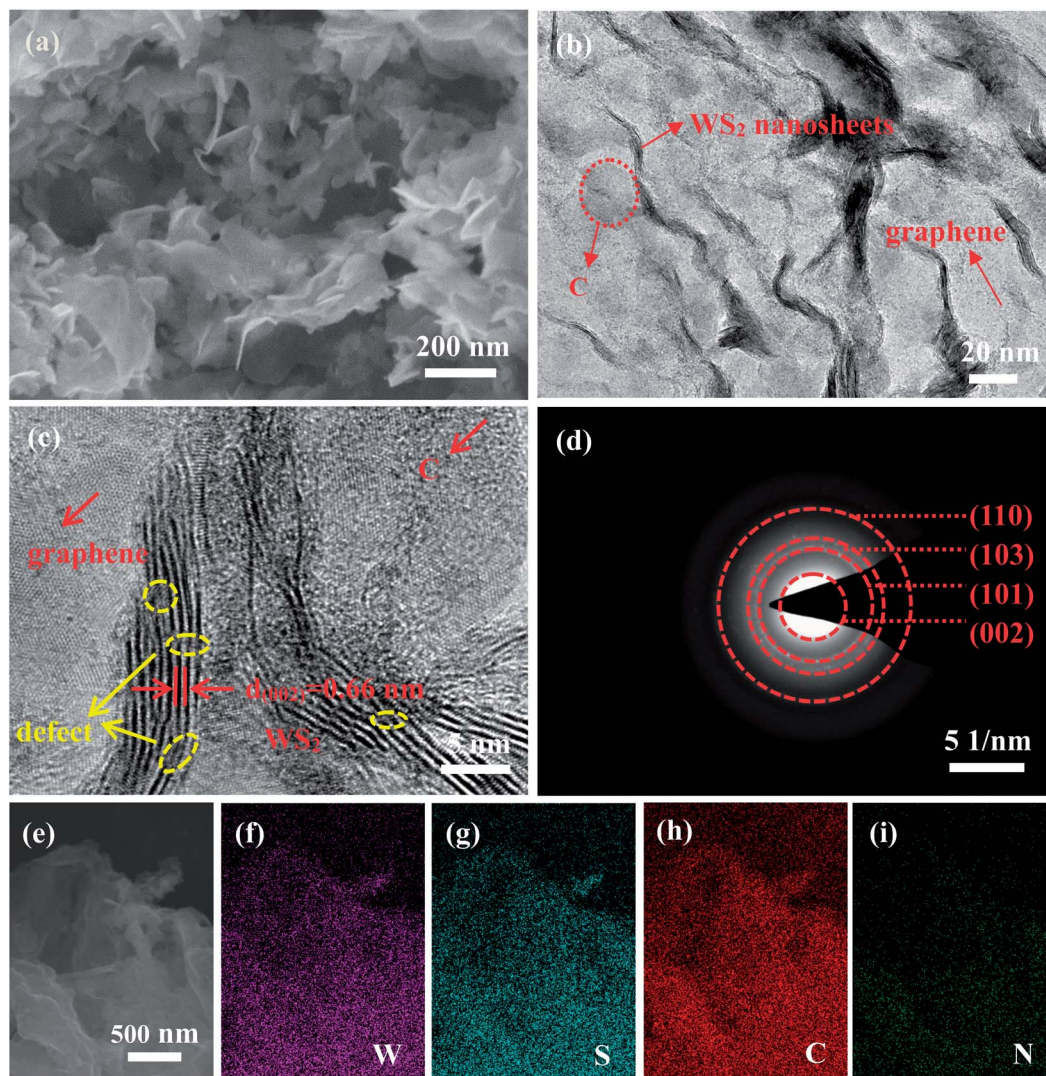
Fig. 2 SEM (a), TEM (b), HRTEM (c), SAED (d), low magnification SEM image (e) and the corresponding elemental mappings of EDS mappings W (f), S (g), C (h) and N (i) of O-DS-WS$_2$/NSG-800, respectively.

nanocomposites, the samples annealed with the different temperatures have been shown in Fig. S4a and b.† It is found that the O-DS-WS$_2$/NSG-650 exhibits the 3D hierarchical sheet-like morphology consistent with that of O-DS-WS$_2$/NSG-800, while as the heat treatment temperature increases to 950 °C, the 3D hierarchical of O-DS-WS$_2$/NSG-950 sheet-like morphology is destroyed to cause the serious aggregation.

The crystal structure of the as-synthesized nanocomposites was first detected by XRD. As shown in Fig. 3a, the XRD patterns of the prepared nanocomposites under different conditions are quite similar. The characteristic diffraction peaks at $2\theta = 14.3°$, 28.9°, 33.6°, 14.3°, 39.6°, 49.8°, 58.5°, 60.5° and 69.1°, are indexed to (002), (004), (101), (103), (006), (105), (110), (112) and (201) plane, respectively, which is in good agreement with the WS$_2$ hexagonal phase (JCPDS card no. 84-1398). The broad diffraction peak located at around $2\theta = 25°$ in the XRD pattern of O-DS-WS$_2$/NSG nanocomposites can be ascribed to the (002) plane of graphitic carbon. In addition, XRD patterns of NSG and

WS$_2$/SG-800 (Fig. S5a and b†) corresponds to the characteristic diffraction peaks of graphitic carbon and 2H-WS$_2$, respectively. Moreover, TGA was carried out to determine the content of WS$_2$ in the O-DS-WS$_2$/NSG nanocomposites under different temperatures (Fig. 3b). For the pristine WS$_2$, the weight loss of about 6.5 wt% represents that WS$_2$ is oxidized to WO$_3$ and SO$_2$, which consistent with theoretically calculated values. For the O-DS-WS$_2$/NSG nanocomposites, the first stage of weight loss below approximately 100 °C is attributed to the removal of free water and physically adsorbed water, and the weight loss above 100 °C corresponds to the oxidation of NSG and WS$_2$.[22,40] According to calculation, the WS$_2$ content in the O-DS-WS$_2$/NSG-650, O-DS-WS$_2$/NSG-800, O-DS-WS$_2$/NSG-950 is 53.4 wt%, 64.9 wt% and 79.6 wt%, respectively. Raman spectrum was performed to further characterize the structure of WS$_2$ and actual carbon. As shown in Fig. 3c and d, the two distinct peaks detected at 349.1 and 415.4 cm^{-1} is E$_{2g}$ and A$_{1g}$ vibration modes of WS$_2$, respectively, which are the characteristic peaks of WS$_2$.[41]
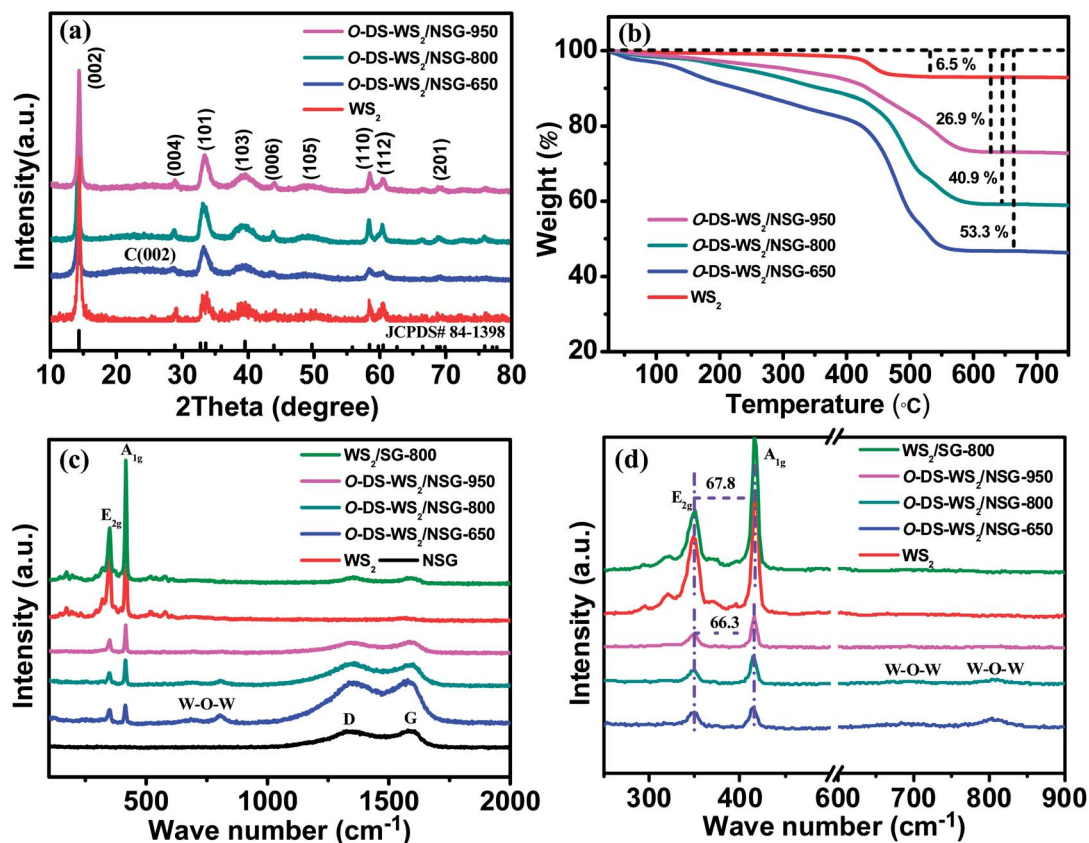
Fig. 3 XRD patterns (a), TGA curves (b) and Raman spectra (c and d) of O-DS-WS$_2$/NSG-800 and its control samples, respectively.

Whether the WS$_2$ nanosheets get thinner after coupling can be acknowledged by Raman spectroscopy as well.[35] As shown in Fig. 3d and S6,† the distance between E$_{2g}$ and A$_{1g}$ peaks of the O-DS-WS$_2$/NSG and O-DS-WS$_2$/NC-800 nanocomposites is about 66.3 cm^{-1}, which is smaller than that of pristine WS$_2$ and WS$_2$/SG-800 with 67.8 cm^{-1}, suggesting the thinner WS$_2$ nanosheets in O-DS-WS$_2$/NSG and O-DS-WS$_2$/NC-800. The peaks appeared at around 1348.1 and 1588.2 cm^{-1} are characteristic peaks of carbon, representing the disorder carbon (D-band) and graphitic carbon (G-band), respectively.[42] At the same time, two peaks appear at 683.8 and 804.6 cm^{-1} could be assigned to the W–O–W bonds for O-DS-WS$_2$/NSG-650, O-DS-WS$_2$/NSG-800, O-DS-WS$_2$/NSG-950, and O-DS-WS$_2$/NC-800.[43]

To analyze the pore properties of the obtained samples, the N$_2$ adsorption–desorption technique was performed. In Fig. 4a–d, all of the adsorption and desorption isothermal curves exhibit the IV-type with remarkable hysteresis, indicating the existence of mesoporous structure in the NSG and O-DS-WS$_2$/NSG,[44,45] which is further proved by the pore size distributions curves (Fig. 4a–d inset). Based on the Brunauer–Emmett–Teller (BET) calculation method, the specific surface area value of the O-DS-WS$_2$/NSG-800 (186.5 m^2 g^{-1}) exceeds that of pristine WS$_2$ (14.2 m^2 g^{-1}) (Fig. S7†) and NSG (162.4 m^2 g^{-1}), which is likely attributed to the formation of 3D hierarchical framework *via* the 2D graphene and 2D few-layer WS$_2$ nanosheets. Lager specific surface area and abundant pore structures not only could

accommodate volume changes during repeated charge–discharge process, but also favor the Li$^+$ diffusion and permeation of the electrolyte as well as provide abundant electrochemical active sites.[4,46] By compared, the specific surface area of O-DS-WS$_2$/NSG-650 is the largest, and the specific surface area of the O-DS-WS$_2$/NSG-950 is the smallest (merely 6.4 m^2 g^{-1}).

XPS measurements were performed to further study the elemental compositions and chemical valence states. The XPS survey spectrum of the O-DS-WS$_2$/NSG-800 (Fig. 5a) confirms the existence of W, S, C, and N elements. For the high-resolution S 2p spectra (Fig. 5b), there are two peaks located at 161.6 and 162.7 eV, corresponding to S 2p$_{3/2}$ and S 2p$_{1/2}$, respectively, indicating the existence of S^{2-} in WS$_2$.[47] The peak at 168.0 eV in O-DS-WS$_2$/NSG-800 is assigned to SO$_4^{2-}$, which attributed to the oxidation of divalent sulfide ions.[48] Five C types (Fig. 5c), including C–C (284.4 eV), C–N (284.8 eV), C–S–C (285.2 eV), C=N (286.1 eV) and C=O (288.5 eV), could be distinguished from the C 1s spectrum, indicating the successful introduction of N and S atoms into the graphene. The XPS N1s spectrum in Fig. 5d is fitted to four peaks centred at about 397.5, 398.7, 400.3 and 401.4 eV, which corresponds to pyridinic N, pyrrolic N, graphitic N and oxidized N, respectively.[49–51] For the W 4f spectrum in Fig. 5e, the peaks appear at 31.8, 34.0 and 37.0 eV are assigned to the W 4f$_{7/2}$, W 4f$_{5/2}$ and W 4f$_{3/2}$, respectively, demonstrating the presence of W^{4+} state in the O-DS-WS$_2$/NSG-
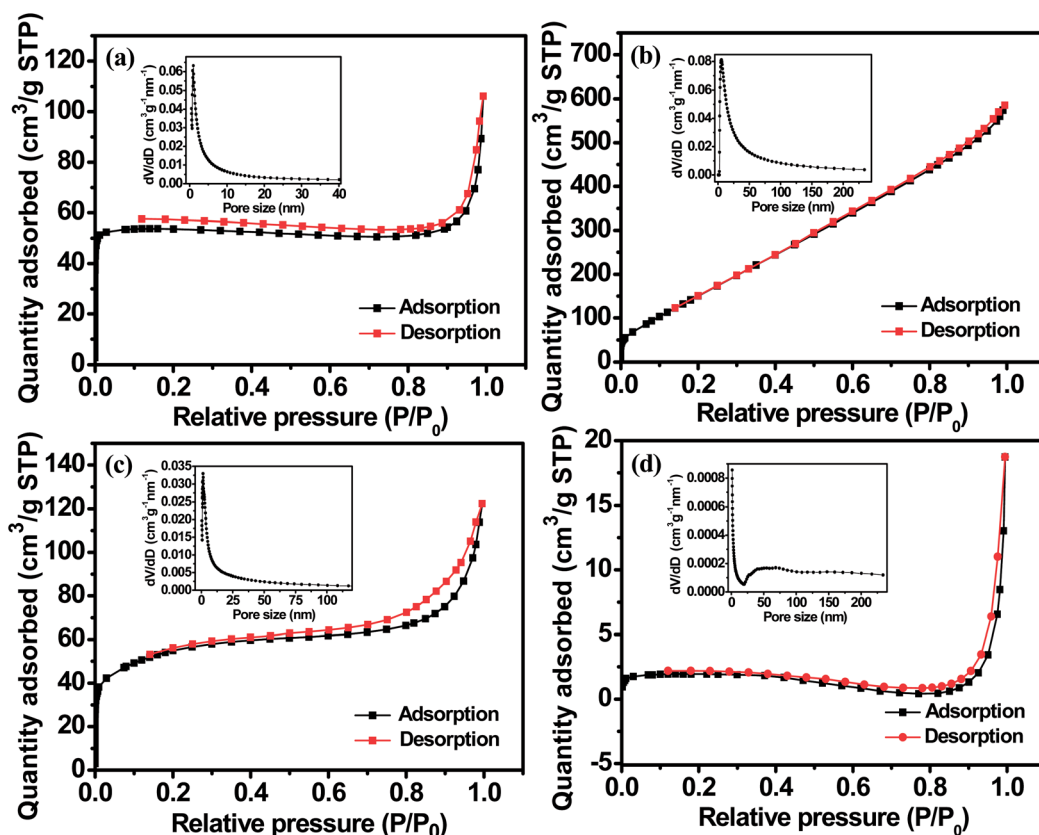
Fig. 4 N$_2$ adsorption and desorption isotherms and pore size distribution of NSG (a), O-DS-WS$_2$/NSG-650 (b), O-DS-WS$_2$/NSG-800 (c) and O-DS-WS$_2$/NSG-950 (d), respectively.

800 nanocomposites. In addition, the binding energy located at 34.8 eV can be attributed to W–O band.[52] Compared with pristine WS$_2$, the binding energies of W in O-DS-WS$_2$/NSG-800 have a negative shift, which could be attributed to the oxygen incorporation in the WS$_2$ lattices, consistent with Raman and TEM results.

Inspired by the unique hierarchical structure, the electrochemical performances of O-DS-WS$_2$/NSG-800 and control samples are preformed. CV testing is firstly conducted to unveil the reaction mechanisms of O-DS-WS$_2$/NSG-800. Fig. 6a presents the first three cycle CV curves with a scanning rate of 0.1 mV s^{-1} to analyze the reaction mechanisms. In the first cathodic scan, the weak peak about 1.41 V is related to the insertion process of Li$^+$ into WS$_2$ lattice to form Li$_x$WS$_2$ (WS$_2$ + xLi$^+$ + xe$^-$ → Li$_x$WS$_2$).[53] The other two peaks located at 0.62 and 0.47 V, which suggests the further reduction of Li$_x$WS$_2$ to form W and the formation of solid electrolyte interface (SEI) layers using the following reaction (Li$_x$WS$_2$ + (4 − x)Li$^+$ + (4 − x) e$^-$ → 2W + 2Li$_2$S).[40,54] In the first anodic sweep, the peak located at 2.43 V corresponds to the process that extraction of Li$^+$ and the conversion of Li$_2$S to S (Li$_2$S + 2e$^-$ → 2Li$^+$ + S).[55] For the 2nd and 3rd cycle, these cathodic peaks are replaced by two new peaks appear at 1.85 and 2.09 V, which is due to significant changes in structure and composition of the electrode after the first cycle.[18] Apart from the first cycle, all peaks coincide well with each other in the following cycles, representing a high

reversibility and cycling stability of O-DS-WS$_2$/NSG-800 electrode. Fig. 6b displays the GDC curves of the O-WS$_2$/NSG-800 electrode for initial three cycles at the current density of 0.1 A g^{-1} at a voltage range of 0.005–3 V. The first cycle discharge and charge specific capacities of O-WS$_2$/NSG-800 are 1721.6 and 1355.3 mA h g^{-1} based on the total mass of the nanocomposites, respectively, with an initial coulombic efficiency (CE) of 78.7%. The large first irreversible capacity is likely due to the formation of SEI film.[35,56,57] Fig. 6c and d comparatively displays the rate performances of the O-DS-WS$_2$/NSG electrode with different temperatures and pristine WS$_2$. Obviously, all O-DS-WS$_2$/NSG electrodes present higher rate capacities than those of pristine WS$_2$ electrode. It is noted that the O-DS-WS$_2$/NSG-800 electrode shows the best rate performances compared with O-DS-WS$_2$/NSG-650 and O-DS-WS$_2$/NSG-950, and delivers the reversible specific capacities of 1082.9, 952.3, 789.2, 632.0, 558.4 and 408.1 mA h g^{-1} at the current densities of 0.1, 0.2, 0.5, 1, 2 and 5 A g^{-1}, respectively. But the reversible specific capacities of pristine WS$_2$ merely are 491.9, 477.4, 395.9, 270.9, 161.1 and 76.7 mA h g^{-1} at the same current densities, respectively. More importantly, when the current density is reset to 0.1 A g^{-1} again, the reversible specific capacity of O-DS-WS$_2$/NSG-800 still can go back to 1048.4 mA h g^{-1} and keep stable, showing a great rate retention. Fig. 6e depicts the cycling stability measurement results of pristine WS$_2$ and O-DS-WS$_2$/NSG anodes at the current density of 0.5 A g^{-1}. After 300 cycles,
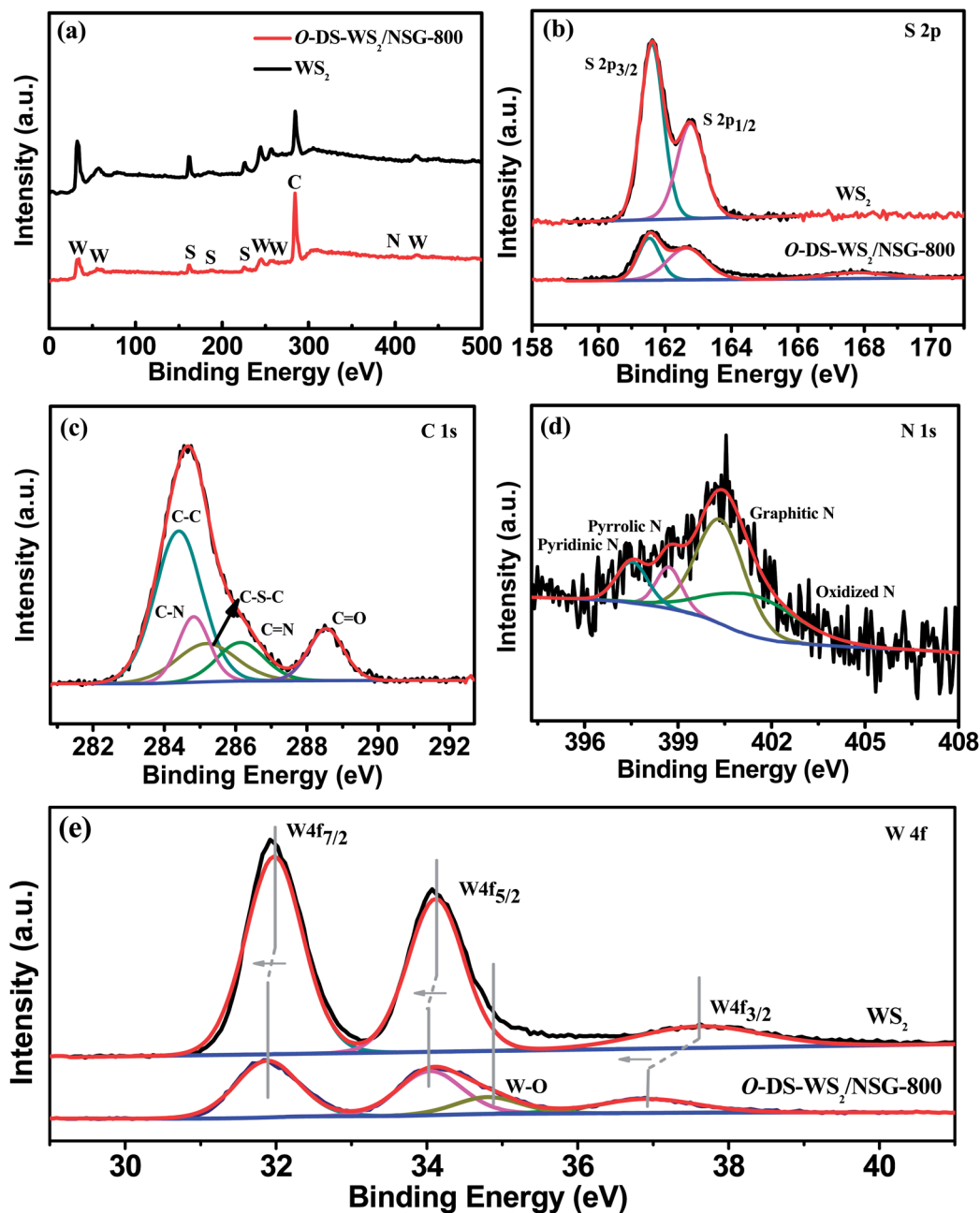
Fig. 5 XPS full survey spectra of pristine WS_2 and O-DS-WS_2/NSG-800 (a). High resolution XPS spectra of pristine WS_2 and O-DS-WS_2/NSG-800, S 2p (b) and W 4f (e). High resolution XPS spectra of O-DS-WS_2/NSG-800, C 1s (c) and N 1s (d), respectively.

the reversible specific capacities of O-DS-WS_2/NSG-800 anode still maintain 721.1 mA h g^{-1} with capacity fading of 14.9% and the CE of 99.6%, which is larger than most previously reported WS_2-based anode materials for LIBs over a potential window of 0.01–3.0 V (Table S1†).[19,53,55] Its result indicates that O-DS-WS_2/NSG-800 possesses significant advantages and the appropriate mass loading for the battery assembly. Generally, the total theoretical specific capacity of nanocomposite can be calculated by the proportion of each component based on the following equation:

$$C_{total} = C_{WS_2} wt_{WS_2}\% + C_{carbon} wt_{carbon}\%$$

Therefore, the theoretical specific capacity of O-DS-WS_2/NSG-650, O-DS-WS_2/NSG-800 and O-DS-WS_2/NSG-950 is 404.4, 411.4 and 420.2 mA h g^{-1}, respectively. In this work, the actual specific capacity after 300 cycles at the current density of 0.5 A g^{-1} of the above three electrodes is larger than their theoretical specific capacity by 192.5, 309.7 and 2 mA h g^{-1}, respectively, and the excess specific capacities may be attributed to the advantages of each single component and synergistic effects among them.

By dissecting O-DS-WS_2/NSG-800 cell after 300 cycles cycling, it is found that the color of separator do not almost change

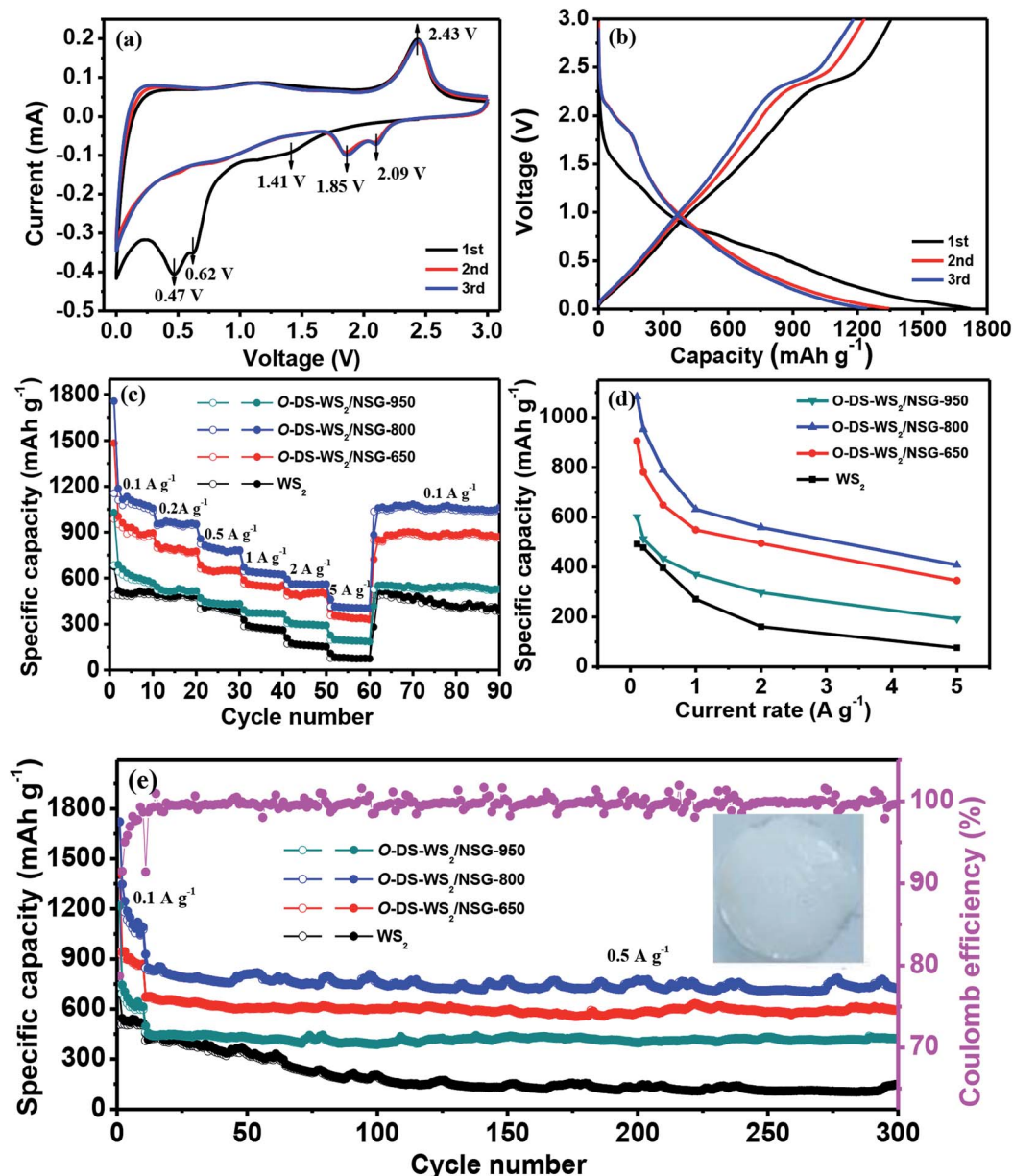Fig. 6 CV curves at 0.1 mV s^{-1} (a) and GDC profiles at 0.1 A g^{-1} (b) of O-DS–WS$_2$/NSG-800 electrodes. Rate capacities (c and d) and cycling properties (e), respectively.

(Fig. 6e inset), indicating the good adsorption and conversion of the polysulfide by O-DS-WS$_2$/NSG-800.[58] Although the 3D hierarchical structure of the O-DS-WS$_2$/NSG-800 electrode has been maintained, the WS$_2$ nanosheets cannot be observed, which may be attributed to the partial hierarchical structural collapse and SEI film covering of the electrode surface (Fig. 7a). However, some few-layer WS$_2$ nanosheets still can be observed in the TEM (Fig. 7b). In addition, the O-DS-WS$_2$/NSG-650 and O-DS-WS$_2$/NSG-950 electrodes also exhibit good cycling stability, but their reversible specific capacities are lower with about 591.8 and 420.1 mA h g^{-1}, respectively. The low electrochemical performance of O-DS-WS$_2$/NSG-650 and O-DS-WS$_2$/NSG-950 may be attributed to the low WS$_2$ content and serious aggregation of

active materials, respectively. For pristine WS$_2$ electrode, it exhibits a severe fading and decays rapidly to 148.8 mA h g^{-1} after 300 cycles. Furthermore, we also investigate the contribution of NSG to the electrochemical properties of O-DS-WS$_2$/NSG-800 electrode, and find that the graphene's contribution to capacity is very small (Fig. S8a and †). As shown in Fig. S9 and S10,† the electrochemical performances in term of specific capacity, cycling stability and rate performance of O-DS-WS$_2$/NC-800 electrode are much better than those of WS$_2$/SG-800 electrode, but lower than those of O-DS-WS$_2$/NSG-800 electrode, proving the merit of few-layer WS$_2$ nanosheets and oxygen incorporation and sulphur defects with more lithium storage active sites.
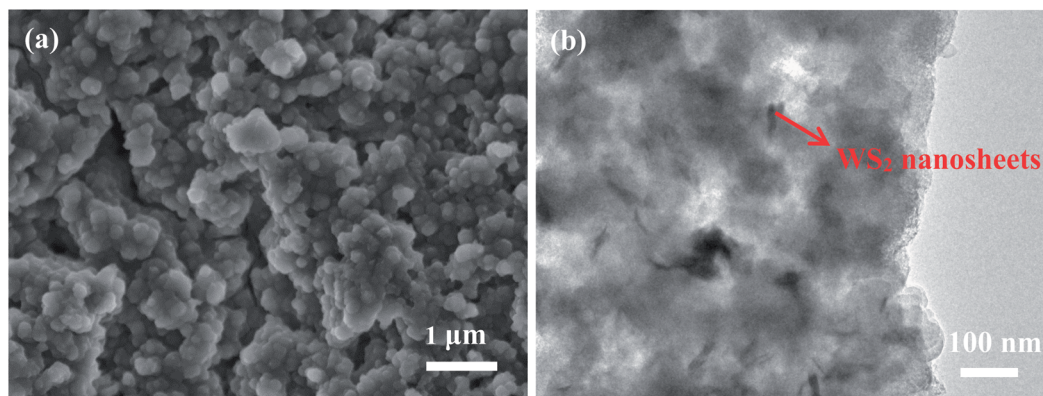
Fig. 7 SEM (a) and TEM (b) of O-DS-WS$_2$/NSG-800 electrode after 300 cycles, respectively.

Electrochemical kinetics of electrode was further studied by EIS measurements. Fig. 8a and S11† exhibit the Nyquist profiles of the pristine WS$_2$, NSG, O-DS-WS$_2$/NSG with various treatment temperatures and WS$_2$/SG-800 before cycling, respectively, and the corresponding equivalent circuit diagram. The electrochemical impedance spectrum is composed of a semicircular curve in the mid-high frequency and a straight line in low frequency region.[8,59] The fitted impedance values from the experimental Nyquist plots are listed in Table S2 (ESI†). Apparently, both R_f and R_{ct} of O-DS-WS$_2$/NSG electrodes are lower than those of pristine WS$_2$ electrode, indicating that the O-DS-WS$_2$/NSG electrodes have the stable SEI layer and faster charge transfer process. In addition, the R_{ct} value of O-DS-WS$_2$/NSG-650, O-DS-WS$_2$/NSG-800 and O-DS-WS$_2$/NSG-950 increase successively, which is due to the decreased carbon contents caused calcination temperature. In the low frequency region, the slopes of the straight line of the O-DS-WS$_2$/NSG nanocomposites are bigger than that of the pristine WS$_2$, indicating the faster diffusion rate. Li$^+$ diffusion rate is further evaluated by Li$^+$ diffusion coefficient (D) based on the eqn (1) and (2) (ESI†) and Fig. 8b (plots about Z' versus $\omega^{-1/2}$). According to calculation, the D value of the pristine WS$_2$ and O-DS-WS$_2$/NSG-800 electrode is 2.99×10^{-14} and 2.10×10^{-13} cm^2 s^{-1}, respectively, which indicates introduction of graphene can

effectively enhance Li$^+$ diffusion kinetics of the nanocomposites.[8,32,35]

The charge storage behavior and reaction kinetics of O-DS-WS$_2$/NSG-800 electrode are further investigated based on CV tests at different sweep rates from 0.1 to 5.0 mV s^{-1} (Fig. 9a). According to previous reports, the total charge storage behavior consists of two parts, including surface capacitance contribution and diffusion control processes, which can be evaluated according to the eqn (1) and (2):[60]

$$i = av^b \qquad (1)$$

$$\log(i) = \log a + b \log(v) \qquad (2)$$

where b is adjustable parameters between 0.5 and 1, it can be determined by the slope of $\log(i)$–$\log(v)$. When b is 0.5 and 1.0, it is controlled by the diffusion-controlled process and the capacitance controlled process, respectively.[61] Fig. 9b shows the relation between $\log(i)$–$\log(v)$ at different oxidation and reduction peaks, calculated b values is 0.68 and 0.81 for cathodic and anodic peaks, respectively, suggesting the coexist of pseudocapacitance and ion diffusion processes. The value of capacitance contribution ratios in O-DS-WS$_2$/NSG-800 electrode at a certain sweep speed can be further evaluated through the following eqn (3):
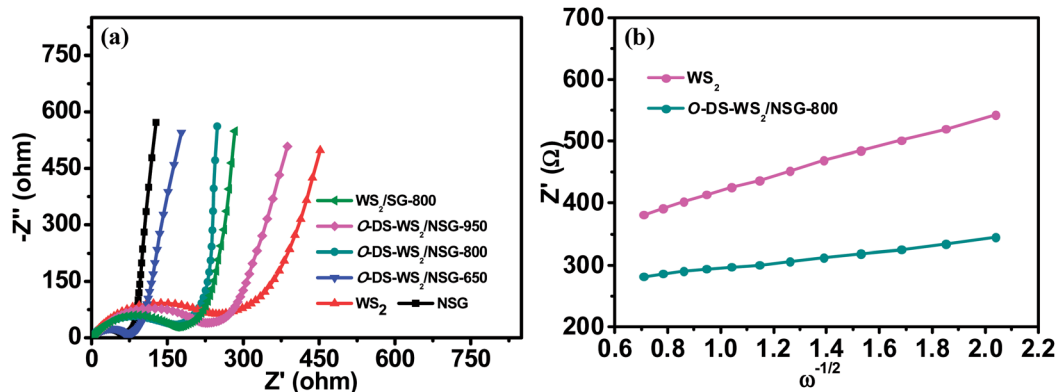

Fig. 8 Nyquist plots (a) and the relationship between Z' and $\omega^{-1/2}$ in the low frequency region (b), respectively.
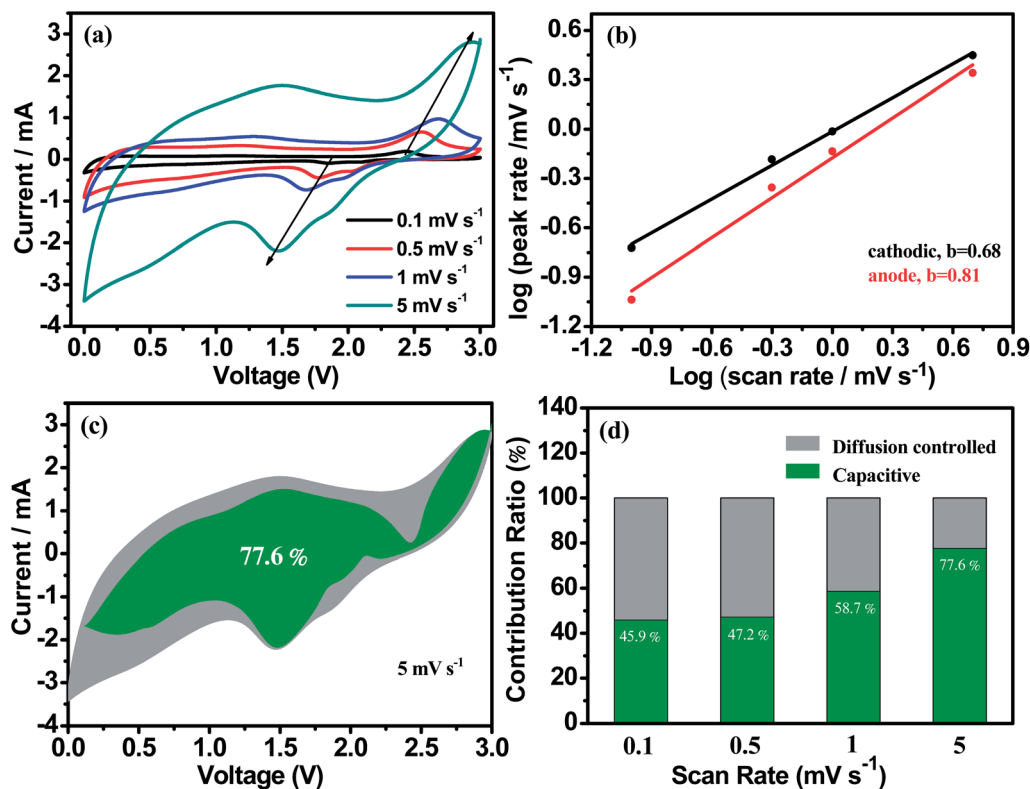
Fig. 9 Electrochemical kinetics investigation of O-DS-WS$_2$/NSG-800 electrode. CV curves at various scan rates (a). Determination of the b-value according to peak current and scan rate (b). Contribution ratio of the capacitive at a scan rate of 5 mV s^{-1} (c) and contribution ratio of the capacitive and diffusion behaviors at various scan rates (d), respectively.

$$i(V) = k_1 v + k_2 v^{1/2} \tag{3}$$

where k_1 and k_2 is the constants of the capacitance contribution and diffusion control, respectively. The k_1 value can be determined from by linearly fitting the $i(V)/v_{1/2}$ vs. $k_1 v_{1/2}$, and then the capacitive contribution ($i(V) = k_1 v$) is separated from the total measured current. The capacitive contribution of O-DS-WS$_2$/NSG-800 electrode accounts for 77.6% of the total capacity at 5 mV s^{-1} (Fig. 9c). The capacitive contributions of the O-DS-WS$_2$/NSG-800 electrode increases gradually as the scan rate rises from 0.1 to 5 mV s^{-1}, finally achieving the maximum value of 77.6% (Fig. 9d). This great capacitive behavior might be ascribed to the abundant defect and graphene support in the O-DS-WS$_2$/NSG, thus resulting in high rate capability and superior cycling performance.

Thus, the superior electrochemical performances in the LIBs of O-DS-WS$_2$/NSG-800 electrode with synergistically structural and electronic modulations can be attributed to the following aspects: (i) O-DS-WS$_2$ nanosheets embedded into NSG frameworks can form a porous 3D hierarchical architecture, which can provide the large electrode/electrolyte contact areas and hetero-interfacial areas between them, thus promoting the diffusion of Li$^+$ and multiplying active sites for Li$^+$ intercalation (Fig. 10); (ii) 3D hierarchical NSG can not only improve the conductivity of the electrode and facilitate the transport of electrons and ions, but also relieve volume effect as well as impress aggregation of WS$_2$ nanosheets during repeated charge–discharge process; (iii) few-layer WS$_2$ nanosheets with oxygen incorporation and sulphur defect can afford more active sites to lithium adsorption.
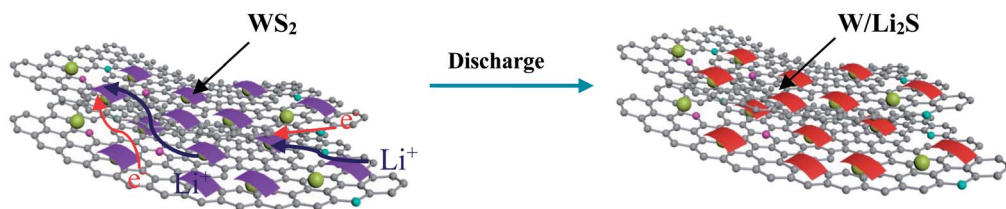

Fig. 10 Schematic illustration of the charge and discharge mechanism of O-DS-WS$_2$/NSG-800.

Conclusions

The hierarchical few-layer O-DS-WS$_2$ nanosheets embedded into the NSG framework (O-DS-WS$_2$/NSG-800) was fabricated successfully *via* a simple one-step heating treatment method. As an anode material for LIBs, the O-DS-WS$_2$/NSG-800 electrode exhibits excellent reversible capacity, outstanding rate capability and superior cycling stability (721.1 mA h g^{-1}) with the small capacity degradation after 300 cycles under current rate of 0.5 A g^{-1}. The superior electrochemical performances demonstrate the strong synergistic effect between highly active 2D WS$_2$ and 2D NSG nanosheet. More importantly, few-layer WS$_2$ nanosheets with oxygen incorporation and sulphur defect can not only introduce abundant active sites for Li$^+$ storage but also increase the intrinsic electrical conductivity. Therefore, our work shows a feasible and effective method for designing and fabricating high-performance and long-life anode materials for LIBs.

Conflicts of interest

There are no conflicts to declare.

Acknowledgements

Notes and references

1 W.-J. Liu, H. Jiang and H.-Q. Yu, *Energy Environ. Sci.*, 2019, **12**, 1751–1779.
2 T. M. Gür, *Energy Environ. Sci.*, 2018, **11**, 2696–2767.
3 J. H. Um, K. Palanisamy, M. Jeong, H. Kim and W.-S. Yoon, *ACS Nano*, 2019, **13**, 5674–5685.
4 X. Zhao, D. Luo, Y. Wang and Z.-H. Liu, *Nano Res.*, 2019, **12**, 2872–2880.
5 K. Liang, K. Marcus, S. Zhang, L. Zhou, Y. Li, S. T. De Oliveira, N. Orlovskaya, Y.-H. Sohn and Y. Yang, *Adv. Energy Mater.*, 2017, **7**, 1701309.
6 S. Zhao, Z. Wang, Y. He, H. Jiang, Y. W. Harn, X. Liu, C. Su, H. Jin, Y. Li, S. Wang, Q. Shen and Z. Lin, *Adv. Energy Mater.*, 2019, **9**, 1901093.
7 H. Shi, Z. Fang, X. Zhang, F. Li, Y. Tang, Y. Zhou, P. Wu and G. Yu, *Nano Lett.*, 2018, **18**, 3193–3198.
8 X. Zhao, G. Wang, X. Liu, X. Zheng and H. Wang, *Nano Res.*, 2018, **11**, 3603–3618.
9 Y. Jiang, D. Song, J. Wu, Z. Wang, S. Huang, Y. Xu, Z. Chen, B. Zhao and J. Zhang, *ACS Nano*, 2019, **13**, 9100–9111.
10 J. Xia, L. Liu, J. Xie, H. Yan, Y. Yuan, M. Chen, C. Huang, Y. Zhang, S. Nie and X. Wang, *Electrochim. Acta*, 2018, **269**, 452–461.
11 X. Xu, Z. Meng, X. Zhu, S. Zhang and W.-Q. Han, *J. Power Sources*, 2018, **380**, 12–17.
12 M. Mao, C. Cui, M. Wu, M. Zhang, T. Gao, X. Fan, J. Chen, T. Wang, J. Ma and C. Wang, *Nano Energy*, 2018, **45**, 346–352.
13 H.-C. Wang, Z. Cui, C.-Y. Fan, S.-Y. Liu, Y.-H. Shi, X.-L. Wu and J.-P. Zhang, *Chem.–Eur. J.*, 2018, **24**, 6798–6803.
14 Y. Liu, W. Wang, Y. Wang and X. Peng, *Nano Energy*, 2014, **7**, 25–32.
15 C. Sun, J. Zhang, J. Ma, P. Liu, D. Gao, K. Tao and D. Xue, *J. Mater. Chem. A*, 2016, **4**, 11234–11238.
16 H.-E. Wang, X. Li, N. Qin, X. Zhao, H. Cheng, G. Cao and W. Zhang, *J. Mater. Chem. A*, 2019, **7**, 12068–12074.
17 J. Zhang, L. Yu and X. W. D. Lou, *Nano Res.*, 2017, **10**, 4298–4304.
18 G. Huang, H. Liu, S. Wang, X. Yang, B. Liu, H. Chen and M. Xu, *J. Mater. Chem. A*, 2015, **3**, 24128–24138.
19 J. Li, X. Shi, J. Fang, J. Li and Z. Zhang, *ChemNanoMat*, 2016, **2**, 997–1002.
20 Y. Song, J. Liao, C. Chen, J. Yang, J. Chen, F. Gong, S. Wang, Z. Xu and M. Wu, *Carbon*, 2019, **142**, 697–706.
21 C. Wu, X. Zeng, P. He, L. Chen and W. Wei, *Adv. Mater. Interfaces*, 2018, **5**, 1701080.
22 J. Ren, Z. Wang, F. Yang, R.-P. Ren and Y.-K. Lv, *Electrochim. Acta*, 2018, **267**, 133–140.
23 W. Ai, Z. Luo, J. Jiang, J. Zhu, Z. Du, Z. Fan, L. Xie, H. Zhang, W. Huang and T. Yu, *Adv. Mater.*, 2014, **26**, 6186–6192.
24 Y. Zhang, N. Song, J. He, R. Chen and X. Li, *Nano Lett.*, 2019, **19**, 512–519.
25 X. Xu, X. Yan, Z. Zhong, L. Kang and J. Yao, *Carbon*, 2019, **145**, 311–320.
26 M. Liu, C. Zhang, J. Su, X. Chen, T. Ma, T. Huang and A. Yu, *ACS Appl. Mater. Interfaces*, 2019, **11**, 20788–20795.
27 K. Chen, X. Wang, G. Wang, B. Wang, X. Liu, J. Bai and H. Wang, *Chem. Eng. J.*, 2018, **347**, 552–562.
28 K. Yao, Z. Xu, J. Huang, M. Ma, L. Fu, X. Shen, J. Li and M. Fu, *Small*, 2019, **15**, 1805405.
29 B. Chen, H. Lu, N. Zhao, C. Shi, E. Liu, C. He and L. Ma, *J. Power Sources*, 2018, **387**, 16–23.
30 H. Liu, Y. Tang, W. Zhao, W. Ding, J. Xu, C. Liang, Z. Zhang, T. Lin and F. Huang, *Adv. Mater. Interfaces*, 2018, **5**, 1701261.
31 X. Zhao, H. Wang, G. Zhai and G. Wang, *Chem.–Eur. J.*, 2017, **23**, 7037–7045.
32 Z. Hu, L. Wang, K. Zhang, J. Wang, F. Cheng, Z. Tao and J. Chen, *Angew. Chem.*, 2014, **53**, 12794–12798.
33 X.-H. Zhang, N. Li, J. Wu, Y.-Z. Zheng and X. Tao, *Appl. Catal., B*, 2018, **229**, 227–236.
34 S. Zhang, H. Yang, H. Gao, R. Cao, J. Huang and X. Xu, *ACS Appl. Mater. Interfaces*, 2017, **9**, 23635–23646.
35 W. Ren, H. Zhang, C. Guan and C. Cheng, *Adv. Funct. Mater.*, 2017, **27**, 1702116.
36 Y. Zhang, H. Tao, T. Li, S. Du, J. Li, Y. Zhang and X. Yang, *ACS Appl. Mater. Interfaces*, 2018, **10**, 35206–35215.
37 X. Zhang, Z. Wu and D. Wang, *Electrochim. Acta*, 2018, **281**, 540–548.
38 J. Xie, J. Zhang, S. Li, F. Grote, X. Zhang, H. Zhang, R. Wang, Y. Lei, B. Pan and Y. Xie, *J. Am. Chem. Soc.*, 2013, **135**, 17881–17888.

39 Y. Yan, H. Li, Y. B. Kang, B. Wang, T. Y. Eom, K. Y. Song, S. Nundy, M. W. Cho, C. Kang, P. Nakhanivej, J. Y. Lee, H.-J. Lee and H. S. Park, *J. Mater. Chem. A*, 2019, **7**, 22070–22078.

40 Y. Song, S. Bai, L. Zhu, M. Zhao, D. Han, S. Jiang and Y. N. Zhou, *ACS Appl. Mater. Interfaces*, 2018, **10**, 13606–13613.

41 Y. Chen, R. Ren, Z. Wen, S. Ci, J. Chang, S. Mao and J. Chen, *Nano Energy*, 2018, **47**, 66–73.

42 Y. Qi, Y. Cao, X. Meng, J. Cao, X. Li, Q. Hao, W. Lei, Q. Li, J. Li and W. Si, *Sens. Actuators, B*, 2019, **279**, 170–176.

43 T. Li, R. Guo, Y. Luo, F. Li, Z. Liu, L. Meng, Z. Yang, H. Luo and Y. Wan, *Electrochim. Acta*, 2018, **290**, 128–141.

44 Y. Zhao, F. Wang, C. Wang, S. Wang, C. Wang, Z. Zhao, L. Duan, Y. Liu, Y. Wu, W. Li and D. Zhao, *Nano Energy*, 2019, **56**, 426–433.

45 W. Liu, J. Zhang, Z. Bai, G. Jiang, M. Li, K. Feng, L. Yang, Y. Ding, T. Yu, Z. Chen and A. Yu, *Adv. Funct. Mater.*, 2018, **28**, 1706675.

46 C. Hou, Y. Hou, Y. Fan, Y. Zhai, Y. Wang, Z. Sun, R. Fan, F. Dang and J. Wang, *J. Mater. Chem. A*, 2018, **6**, 6967–6976.

47 S. Ratha and C. S. Rout, *ACS Appl. Mater. Interfaces*, 2013, **5**, 11427–11433.

48 L. Yang, X. Zhu, S. Xiong, X. Wu, Y. Shan and P. K. Chu, *ACS Appl. Mater. Interfaces*, 2016, **8**, 13966–13972.

49 Y. Li, H. Wen, J. Yang, Y. Zhou and X. Cheng, *Carbon*, 2019, **142**, 1–12.

50 Y. Yao, Y. Zhu, J. Huang, J. Shen and C. Li, *Electrochim. Acta*, 2018, **271**, 242–251.

51 Z. Lin, G. H. Waller, Y. Liu, M. Liu and C.-p. Wong, *Carbon*, 2013, **53**, 130–136.

52 J. Ren, R.-P. Ren and Y.-K. Lv, *J. Alloys Compd.*, 2019, **784**, 697–703.

53 Y. V. Lim, Z. X. Huang, Y. Wang, F. H. Du, J. Zhang, T. P. Chen, L. K. Ang and H. Y. Yang, *RSC Adv.*, 2016, **6**, 107768–107775.

54 X. Zhang, R. Zhao, Q. Wu, W. Li, C. Shen, L. Ni, H. Yan, G. Diao and M. Chen, *J. Mater. Chem. A*, 2018, **6**, 19004–19012.

55 I. Kim, S. W. Park and D. W. Kim, *Chem. Eng. J.*, 2019, **375**, 122033.

56 X. Wu and S. Yao, *Nano Energy*, 2017, **42**, 143–150.

57 J. Zhang, L. Zhou, Q. Sun, H. Ming, L. Sun, C. Wang, Y. Wu, K. Guan, L. Wang and J. Ming, *Chem.–Eur. J.*, 2019, **25**, 8813–8819.

58 W. G. Lim, S. Kim, C. Jo and J. Lee, *Angew. Chem., Int. Ed.*, 2019, **58**, 18746–18757.

59 Y. Wang, Z. Chen, T. Lei, Y. Ai, Z. Peng, X. Yan, H. Li, J. Zhang, Z. M. Wang and Y.-L. Chu, *Adv. Energy Mater.*, 2018, **8**, 1703453.

60 X. Li, W. Zhang, J. Cai, H. Yan, M. Cui, G. Wu and M. Li, *Nano Energy*, 2019, **62**, 239–249.

61 Y. Liu, Z. Chen, H. Jia, H. Xu, M. Liu and R. Wu, *ACS Nano*, 2019, **13**, 6113–6124.